Intrinsic thermal conductivity of ZrC from low to ultrahigh temperatures: A critical revisit

Janak Tiwari ⬤ and Tianli Feng ⬤ *
Department of Mechanical Engineering, University of Utah, Salt Lake City, Utah 84112, USA

Current phonon transport theory based on ground-state calculations has been successful in predicting thermal conductivity at room and medium temperatures but may misrepresent behavior at high temperatures. In this work, we predict the thermal conductivity (κ) of ZrC including electronic and phonon contributions from 300 to 3500 K, by including high-order phonon scattering; lattice expansion; temperature-dependent (TD) second-, third-, and fourth-order force constants (2FC, 3FC, and 4FC); and interband phonon conduction by using first principles. For the phonon transport, we find that four-phonon scattering (4ph) significantly reduces the phonon thermal conductivity (κ_{ph}), by as much as $\sim$75% at 3500 K. After including 4ph scattering and all other factors, κ_{ph} shows a $\sim T^{-1.5}$ rather than $\sim T^{-1}$ dependence. TD 2FC decreases three-phonon scattering rates but increases 4ph rates by decreasing and increasing the scattering phase spaces, respectively. For 4ph phase space, the TD 2FC flattens phonon bands, and allows more redistribution-4ph processes ($1 + 2 \rightarrow 3 + 4$) to happen. The combination effect of TD 2FC and TD 4FC reduces 4ph rates of acoustic modes but increases those of optical modes. The TD 3FC and 4FC decrease the phonon scattering cross section and increase the κ_{ph} significantly (by 52% at 3500 K). The contribution from interband (Wigner) phonon conduction is small, even at ultrahigh temperatures. For electronic thermal transport, we find that it is sensitive to and can be changed by 20% by the TD lattice constants. The Lorenz number varies from 1.6 to 3.3×10^{-8} W Ω K^{-2} at different temperatures. The theoretical prediction in the literature overpredicts κ_{ph} (e.g., $\sim$28%) and underpredicts the κ_{el} (e.g., $\sim$38%), resulting in an overall underprediction of κ ($\sim$26% at 1500 K). The impacts of grain size and defects are found to be strong, leading to the lower observed thermal conductivity in experiments.

I. INTRODUCTION

High melting point [1,2], high hardness [3], good thermal conductivity [4,5], excellent chemical stability, good electrical conductivity [5], high strength and stiffness [6,7], and resistance to oxidation [8] even at high temperature make ZrC a suitable material for various high-temperature engineering applications [9–13] such as rocket nozzles, turbine blades, heat shields, cutting tools, refractory materials, armor materials, etc. Furthermore, ZrC is a common material used in the nuclear industry due to its ability to withstand high temperatures and radiation exposure, making it an ideal choice for fuel elements [14,15]. In addition to these applications, ZrC is also used to make electrodes in batteries and fuel cells [16,17]. To effectively design and optimize these applications, a thorough understanding of the underlying heat transfer mechanism of ZrC is necessary.

The study of heat transfer mechanisms in ZrC has been a topic of great interest. Many experimental thermal conductivity data of ZrC from room temperature up to its melting point ($\sim$3700 K) have been reported [4,5,18–23]. However, the measured thermal conductivity data are scattered across the literature. For example, at room temperature, the values vary from as low as 20 W m^{-1} K^{-1} to as high as 40 W m^{-1} K^{-1}, and at 2000 K, they are scattered from 22 to 46 W m^{-1} K^{-1}.

ZrC is a semimetallic material, with the total thermal conductivity (κ) arising from the combined effect of electronic (κ_{el}) and lattice thermal conductivity (κ_{ph}). However, since direct measurement of lattice thermal conductivity is challenging, it is typically derived from the total thermal conductivity by subtracting the electronic contribution by the Wiedemann-Franz law [24,25]. This approach leaves some uncertainty because the Lorenz number (L) is not necessarily $L_0 = 2.44 \times 10^{-8}$ W Ω K^{-2}. Moreover, κ_{ph} is found to be more sensitive to external factors such as defects, grain boundaries, and impurities than κ_{el}, making it further challenging to unveil the intrinsic thermal conductivity directly from the existing experimental data.

Different theoretical studies [26–29] based on molecular dynamics (MD) and density functional theory (DFT) have been done to understand the thermal conductivity of ZrC. Crocombette [26] studied the phonon and electronic thermal conductivity of ZrC from 1000 to 3500 K using molecular dynamics (MD). They further found that the impacts of defects are strong. Although they account for the temperature effect and predict thermal conductivity correctly using MD, they did not discuss intrinsic scattering and fundamental thermal transport mechanisms. Zhou *et al.* found that carbon vacancy [27] and Hf additive [28] greatly suppress the phonon thermal conductivity by using first-principles calculations. However, their results are based on the Debye-Callaway model (of which the accuracy can be questionable) and ignored the higher-order scattering, which is found to be important at

---

*Corresponding author: tianli.feng@utah.edu

elevated temperatures [30,31]. Moreover, their study is focused only on lattice thermal conductivity. Mellan *et al.* [29] predicted the thermal conductivity of ZrC by incorporating both three-phonon scatterings (3ph) and four-phonon scatterings (4ph), as well as phonon renormalization for the second-order force constant. However, their calculations were only based on ground state force constants (GSFCs), which may not be accurate for high-temperature calculations as found in Ref. [32]. In this work, we predict the thermal conductivity of ZrC by including high-order phonon scattering, lattice expansion, and temperature-dependent force constants (TDFCs). We also calculate the off-diagonal (Wigner) thermal conductivity, which is found to be significant for various materials at high temperatures. Additionally, we have analyzed the impact of extrinsic factors such as grain boundary scattering, defect scattering, and impurity scattering on phonon thermal conductivity at different temperatures.

II. METHODOLOGY

ZrC is a semimetallic material with thermal conductivity (κ) being

$$\kappa = \kappa_{\text{ph}} + \kappa_{\text{el}}. \tag{1}$$

Based on the Boltzmann transport equation (BTE), the κ_{ph} can be calculated as

$$\kappa_{\text{ph}}^{\alpha\beta} = \sum_{\lambda} c_{\lambda} v_{\lambda}^{\alpha} v_{\lambda}^{\beta} \tau_{\lambda}^{\text{ph}}, \tag{2}$$

where $\lambda = (\mathbf{q}, \upsilon)$ denotes the phonon mode with wave vector $\mathbf{q}$ and polarization υ. c_{λ} is the specific heat per mode, v_{λ}^{α} and v_{λ}^{β} are phonon group velocities along the α and β directions. $\tau_{\lambda}^{\text{ph}}$ is the phonon relaxation time which can be calculated using $\frac{1}{\tau_{\lambda}^{\text{ph}}} = \frac{1}{\tau_{\lambda}^{\text{ph}-\text{ph}}} + \frac{1}{\tau_{\lambda}^{\text{ph}-i}} + \frac{1}{\tau_{\lambda}^{\text{ph}-\text{el}}}$ where the three terms on the right are phonon-phonon (including 3ph and 4ph), phonon-isotope, and phonon-electron (ph-el) scattering rates, respectively.

Similarly, κ_{el} is calculated based on BTE and Onsager [33] relations as

$$\sigma_{\alpha\beta} = -\frac{e^2 n_s}{V} \sum_{i\mathbf{k}} \frac{df_{i\mathbf{k}}}{d\varepsilon} \upsilon_{i\mathbf{k}}^{\alpha} \upsilon_{i\mathbf{k}}^{\beta} \tau_{i\mathbf{k}}^{\text{el}}, \tag{3}$$

$$[\sigma S] = -\frac{e n_s}{V T} \sum_{i\mathbf{k}} (\varepsilon_{i\mathbf{k}} - \mu) \frac{df_{i\mathbf{k}}}{d\varepsilon} \upsilon_{i\mathbf{k}}^{\alpha} \upsilon_{i\mathbf{k}}^{\beta} \tau_{i\mathbf{k}}^{el}, \tag{4}$$

$$K_{\alpha\beta} = -\frac{n_s}{V T} \sum_{i\mathbf{k}} (\varepsilon_{i\mathbf{k}} - \mu)^2 \frac{df_{i\mathbf{k}}}{d\varepsilon} \upsilon_{i\mathbf{k}}^{\alpha} \upsilon_{i\mathbf{k}}^{\beta} \tau_{i\mathbf{k}}^{\text{el}}. \tag{5}$$

Here, $\sigma_{\alpha\beta}$ and $S_{\alpha\beta}$ denote the electrical conductivity and Seebeck coefficient. $K_{\alpha\beta}$ is used to calculate κ_{el} as $\kappa_{\text{el}} = K - S\sigma S T$. e is the elementary charge, $\mathbf{k}$ is the electronic wave vector at band index i, V is the volume of the primitive cell, and $f_{i\mathbf{k}}$ is Fermi-Dirac distribution. $\varepsilon_{i\mathbf{k}}$ and μ denote electron energy and chemical potential, respectively. $\upsilon_{i\mathbf{k}}$ and $\tau_{i\mathbf{k}}^{\text{el}}$ denote electron velocity and relaxation time and α and β are directional components. The formulation is referred from Refs. [33,34].

Extrinsic scattering rates due to grain boundary ($\tau_{\text{gb},\lambda}^{-1}$) and vacancy ($\tau_{d,\lambda}^{-1}$) are calculated using the formulations shown in Eqs. (6) and (7), respectively.

$$\tau_{\text{gb},\lambda}^{-1} = \frac{v_{\text{ph},\lambda}}{D_{\text{grain}}}. \tag{6}$$

$$\tau_{d,\lambda}^{-1} = 9\frac{\pi}{2} f_v \omega_{\lambda}^2 \text{pDOS}(\omega). \tag{7}$$

Here, λ represents the phonon mode ($\mathbf{q}$, j) with $\mathbf{q}$ and j labeling the phonon wave vector and dispersion branch, respectively. v_{ph} represents the phonon group velocity at λ, and D_{grain} is the grain size. Similarly, f_v represents the concentration of the vacancy. Likewise, ω represents the angular velocities and pDOS(ω) represents the partial density of states of a basis atom. The coefficient 9 in Eq. (7) accounts for the mass and bond loss associated with the defect vacancy [35,36]. More detail on the extrinsic scattering rates calculation can be found in Ref. [37] and the Supplemental Material [38].

Figure 1 shows the computational workflow of the study. The first-principles calculations based on DFT are performed by using the Vienna *ab initio* simulation package (VASP) [39,40], using the projected augmented wave (PAW) [41] method and the Perdew-Burke-Ernzerhof (PBE) [42] functional. ZrC belongs to the *Fm3m* space group and exhibits a cubic fcc structure. The plane-energy cutoff is 500 eV and the energy and force convergence thresholds are 2×10^{-8} eV and 2×10^{-8} eV Å^{-1}, respectively. The relaxed lattice constant is 4.710 Å, which closely resembles the experimental value [2] of 4.694 Å. Harmonic (second-order) force constants (HFCs or 2FCs) are extracted using PHONOPY [43]. The anharmonic force constants (AFCs), including third- (3FC) and fourth-order (4FC), are calculated using the THIRDORDER and FOURTHORDER packages built inside SHENGBTE [44], considering the fourth and second nearest atoms, respectively. In all DFT calculations, supercells of $4 \times 4 \times 4$ (128 atoms) are used with a **k**-point grid of $6 \times 6 \times 6$. Temperature-dependent second-, third-, and fourth-order force constants are obtained by the TDEP method [45,46] with the input being the energy, forces, and stresses of atoms in a randomly displaced supercell lattice at the provided temperature. The effect of the temperature is factored in as a thermal expansion as well as in the displacement of the generated supercells. Three hundred random configurations are found to be sufficient at lower temperatures (300–1000 K), while 500 configurations are needed at higher temperatures (1500–3500 K) to obtain converged force constants.

SHENGBTE [44] is used to solve the BTE and calculate the 3ph and 4ph rates and κ_{ph}. The convergence of SHENGBTE is tested and provided in the Supplemental Material [38]. Specifically, the 3ph calculation converges at a **q**-mesh density of $36 \times 36 \times 36$, and the 3ph + 4ph calculation converges at $12 \times 12 \times 12$, respectively. Different extrinsic scattering rates, such as grain boundary scattering, defect scattering, and isotope scattering, are calculated using their respective formulations. Phonon-electron scattering is calculated using density functional perturbation theory (DFPT) [47–49] and maximally localized Wannier functions using EPW [50–53]. Finally, total scattering rates are obtained by adding all
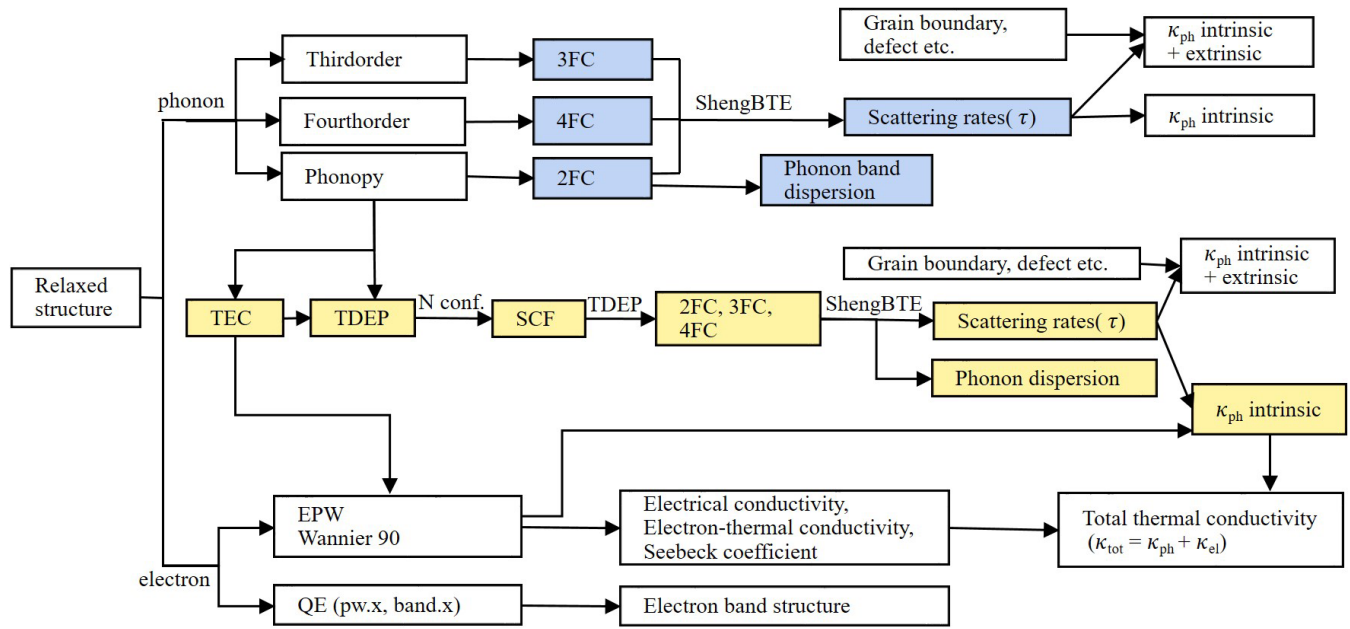
FIG. 1. Computation workflow of this study.

the phonon scattering rates and are used to calculate the intrinsic κ_{ph}.

The electronic contribution to κ is calculated using EPW [50–53] interfaced with QUANTUM ESPRESSO [54,55]. The structure is relaxed with a **k** mesh of $12 \times 12 \times 12$, a kinetic energy cutoff of 200 Ry, and Gaussian smearing with a spreading parameter of 0.002 Ry. Self-consistency is achieved using Davidson iterative diagonalization with a convergence threshold of 10^{-12}. Phonon-electron scattering rates are calculated using a $12 \times 12 \times 12$ **k** mesh. Electron-phonon scattering rates are calculated using a coarse $6 \times 6 \times 6$ **q** mesh and **k** mesh and a fine $60 \times 60 \times 60$ **q** mesh and **k** mesh for convergence. The sp^3 and d entanglements are used for C and Zr, respectively. The electrons' velocities are calculated using WANNIER90 [56] under the EPW package. The Fermi window is selected so that the electron band dispersions obtained using the EPW package and DFT match with each other. Likewise, the outer window is selected so that it includes all the bands of interest. Finally, σ, κ_{el}, and S are calculated.

III. RESULTS AND DISCUSSION

A. Thermal expansion coefficient

The thermal expansion coefficient (TEC) is calculated using quasiharmonic approximation (QHA) with the formalism found in Ref. [60]. As shown in Fig. 2, the predicted TEC (blue curve) deviates from experimental data at high temperatures, which is commonly seen for QHA. To resolve the discrepancy, we replace the constant bulk modulus (229 GPa [4]) in the formalism with temperature-dependent (TD) bulk modulus [57], and the predicted TEC (black dashed curve) agrees better with experimental data. After we include TDFC, the TEC (black solid curve) at high temperature agrees even better with experimental data. It is important to note that the TD bulk modulus tends to increase the slope of TEC with temperature, while TDFC tends to decrease it. Overall, these

findings suggest that utilizing the TD bulk modulus and TDFC is a promising approach for the accurate prediction of TEC at high temperatures.

B. Temperature-dependent phonon band dispersion

The phonon dispersion relations of ZrC at 0, 300, 1000, and 3000 K are shown in Fig. 3, which match well with the experimental data [61,62]. The temperature softening effect in ZrC is not significant. The phonon dispersion calculated from
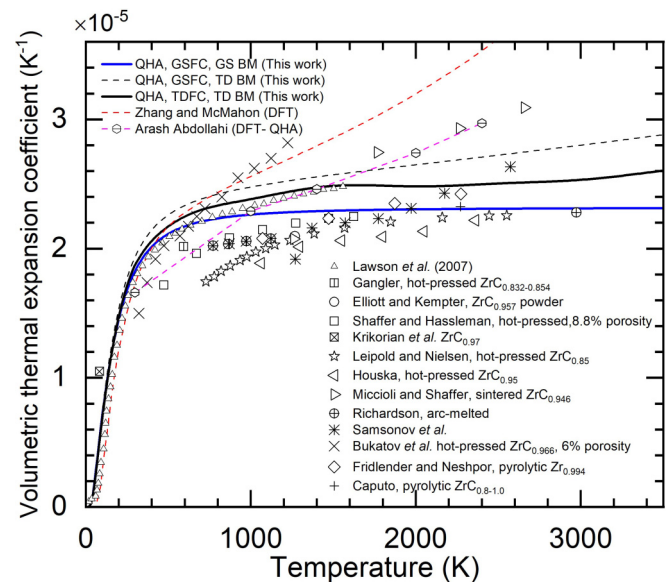

FIG. 2. Predicted volumetric thermal expansion coefficient of ZrC as a function of temperature. The DFT predicted data by Zhang and McMahon [57] and Abdollahi [58], as well as different experimental data (Lawson *et al.* [59] and those reproduced from Jackson and Lee [4]), are included for comparison.
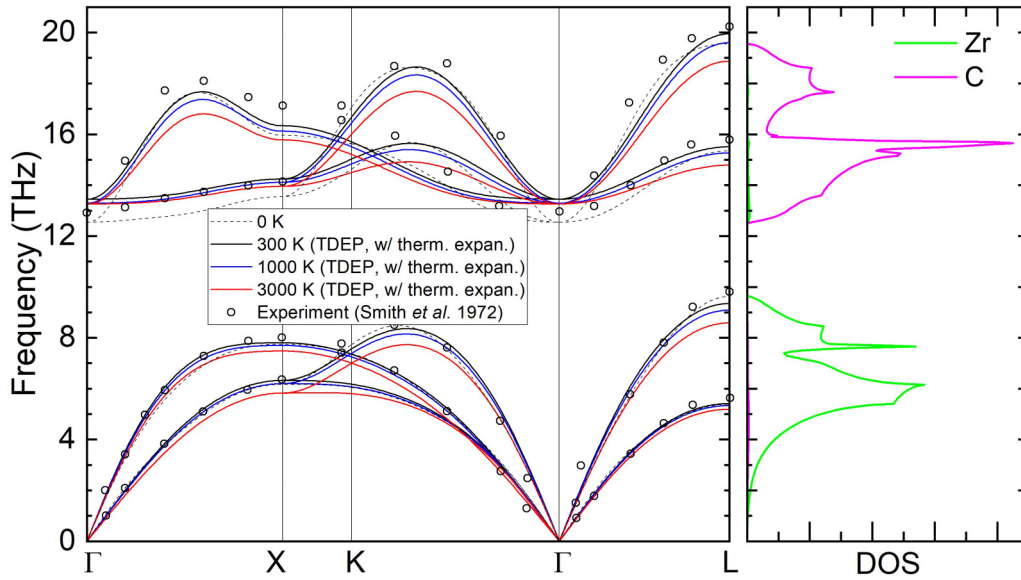
FIG. 3. Phonon dispersion relations of ZrC at 0, 300, 1000, and 3000 K, compared to the experimental data [61,62]. The right side shows the partial density of states of Zr and C at 0 K.

TDEP at finite temperature deviates slightly from the ground state calculations. The partial density of states (PDOS) shows that the heavier metal Zr dominates the acoustic phonon of frequency 0–10 THz, while the lighter element C dominates the optical phonon of frequency 12–20 THz. Since the acoustic phonon modes contribute the most to lattice heat transfer, we can expect that Zr vibration dominates the heat transfer.

C. Scattering rates

The 3ph, 4ph, and ph-el rates, at three different temperatures of 300, 1000, and 3000 K, are presented in Fig. 4. The 3ph dominates throughout all temperatures, and 4ph becomes important at high temperatures, while ph-el is insignificant at all temperatures (even though a very small portion of phonons show high ph-el rates). The 4ph plays a more important role in optical phonons than acoustic phonons, similar to the findings in Si, boron arsenide (BAs), and diamond [30]. The large 4ph rates are due to the large acoustic-optical phonon band gap, which restricts 3ph processes.

Figures 4(a)–4(c) show the impacts of TDFC on 3ph rates at various temperatures. It is seen that TDFC decreases the 3ph rates at all temperatures. One reason is that the TD 2FC changes the phonon dispersion and reduces the 3ph phase space by making the 3ph processes' energy and momentum conservation rules harder to be satisfied, which has been widely discovered in many other materials [63,64]. We explicitly check the 3ph phase spaces of ZrC at 3000 K using ground state (GS) and TD 2FC separately, as shown in Fig. 5(a). It is seen that most modes are reduced even though some are increased. We have also compared the 3ph rates using GS and TD 2FC and found that TD 2FC gives smaller 3ph rates than GS 2FC, as shown in Fig. 5(e). The other reason is that the 3FC is softened by temperature [32]. As seen in Fig. 5(f), using TD 3FC gives slightly smaller 3ph rates than using GS 3FC.

Figures 4(d)–4(f) show the impacts of TDFC on 4ph rates at various temperatures. Interestingly, acoustic 4ph rates decrease while the optical 4ph rates increase when using the TDFC instead of the GSFC. This trend becomes more prominent as the temperature increases. To understand the physical reason behind this phenomenon and tell whether this is induced by the temperature dependence of 2FC or 4FC, we have done the following two comparisons at 3000 K. First, we compare "GS 2FC + TD 4FC" and "TD 2FC + TD 4FC" to isolate the impact of TD 2FC. As shown in Fig. 5(g), TD 2FC results in higher 4ph rates for both acoustic and optical phonons than GS 2FC. This is because TD 2FC flattens both acoustic and optical phonon dispersions, which makes the 4ph energy conservation rule easier to be satisfied, especially for the 4ph redistribution processes ($\lambda_1 + \lambda_2 \rightarrow \lambda_3 + \lambda_4$) where the modes λ_1 and λ_3 sit on the same flat band while the modes λ_2 and λ_4 sit on the other same flat band. This effect is clearly shown in Figs. 5(b)–5(d), which shows the scattering phase space for splitting 4ph processes ($\lambda_1 \rightarrow \lambda_2 + \lambda_3 + \lambda_4$), labeled as "−"; redistribution 4ph processes ($\lambda_1 + \lambda_2 \rightarrow \lambda_3 + \lambda_4$), labeled as "+−"; and recombination 4ph processes ($\lambda_1 + \lambda_2 + \lambda_3 \rightarrow \lambda_4$), labeled as "++". It is seen that TD 2FC significantly increases the scattering phase space. This effect is stronger for optical phonons than acoustic phonons as optical branches are flattened more. Second, we compare the "TD 2FC + GS 4FC" and "TD 2FC + TD 4FC" calculations to isolate the impact of TD 4FC. As seen in Fig. 5(h), using TD 4FC gives smaller 4ph rates for both acoustic and optical phonons. This agrees with the fact that TD 4FC reduces the scattering cross section, as found for UO_2 [32]. In summary, TD 2FC and TD 4FC have competing impacts, with the former increasing 4ph rates while the latter decreases them. The impact of TD 2FC dominates for optical phonons while the impact of TD 4FC dominates for acoustic phonons, which results in an increase of 4ph rates in optical phonon modes and a decrease in acoustic phonon modes.
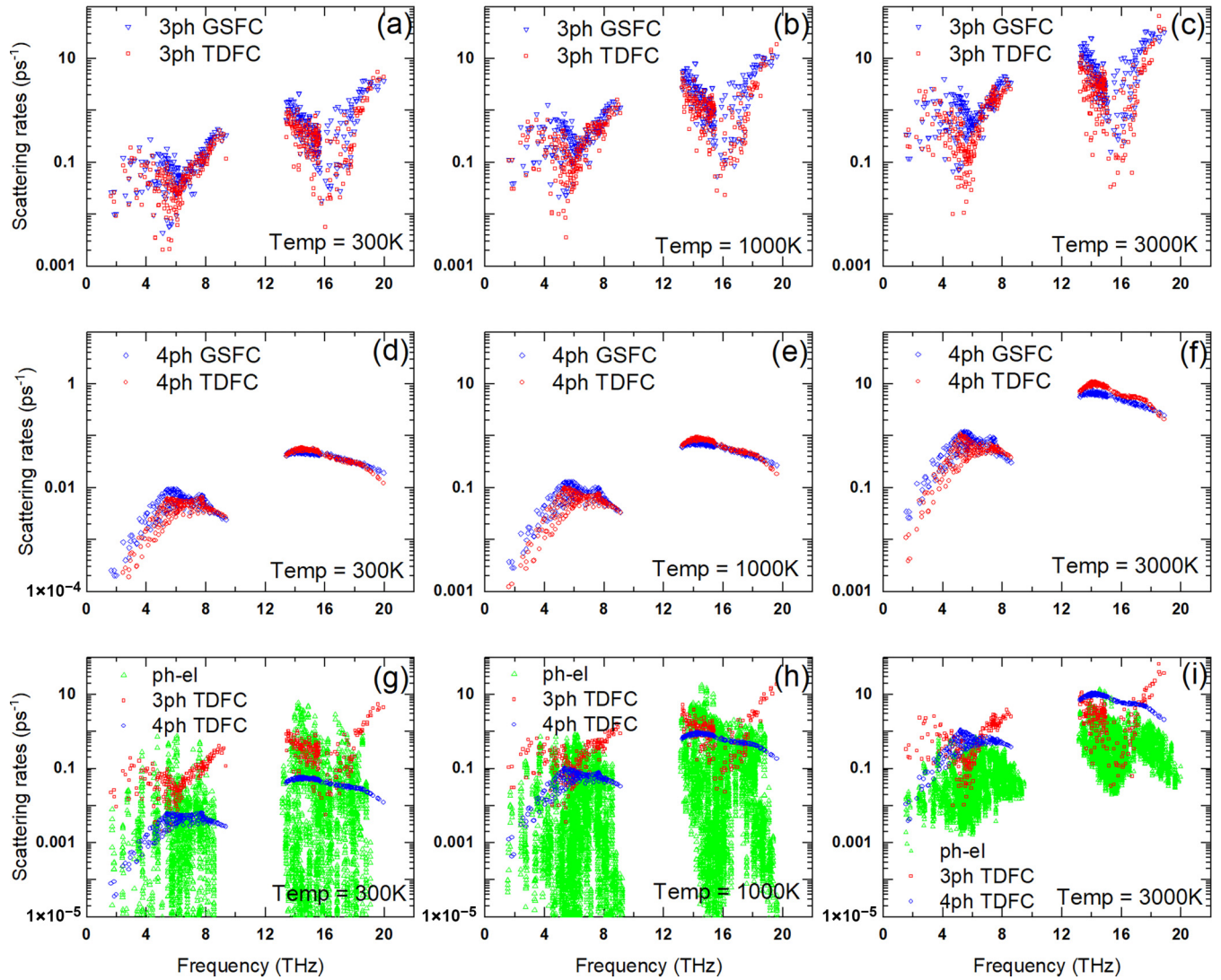
FIG. 4. Comparison of 3ph (a)–(c), 4ph (d)–(f), and ph-el (g)–(i) scattering rates of ZrC at different temperatures. Results by using GSFC and TDFC are compared. GSFC indicates all 2FCs, 3FCs, and 4FCs are at the ground state. TDFC indicates all 2FCs, 3FCs, and 4FCs are temperature dependent.

D. Phonon thermal conductivity calculation

Figure 6 shows the κ_{ph} as a function of temperature, using various force constants. In the following, we track the changes of κ_{ph} at a low (300 K) and a high temperature (3500 K) when we gradually increase the calculation comprehensiveness. First, we calculate the basic 3ph thermal conductivity using GSFC, which gives 56.9 and 6.3 W m^{-1} K^{-1} at 300 and 3500 K, respectively. When we replace the GS 2FC with TD 2FC, κ_{ph} increases by 9% and 33% to 62.1 and 8.4 W m^{-1} K^{-1}, respectively. Then, we include 4ph, and κ_{ph} decreases significantly by 2% and 75% to 61 and 2.1 W m^{-1} K^{-1}, respectively. After that, we replace the GS AFC with the TD AFC, and κ_{ph} increases by 0% and 52% to 61 and 3.2 W m^{-1} K^{-1}, respectively. This increase in κ_{ph} is attributed to the decrease in scattering cross section with increasing temperature [32]. In the end, we add the ph-el scattering, and κ_{ph} slightly decreases by 10% to 55.0 and 2.9 W m^{-1} K^{-1} at 300 and 3500 K, respectively. The inset

illustrates the reduction of thermal conductivity by 4ph as a function of temperature. Further analysis on 4ph using different force constants is provided in the Supplemental Material [38]. The off-diagonal term, calculated from Wigner formalism, is not found to make a significant contribution, unlike in some other materials [65,66]. Although the Wigner contribution increases with temperature, it only reaches a maximum value of 0.2 W m^{-1} K^{-1} at 3500 K, which is much lower than the standard Peierl κ_{ph} of 2.9 W m^{-1} K^{-1} at that temperature. Considering all these intrinsic effects, the κ_{ph} is found to follow a temperature dependence of $\sim T^{-1.5}$ rather than $\sim T^{-1}$.

E. Electronic thermal conductivity calculation

The predicted electrical conductivity (σ) as a function of temperature is shown in Fig. 7. The experimental data along with the DFT prediction from Ref. [29] are also shown for comparison. The σ decreases with temperature monotoni-
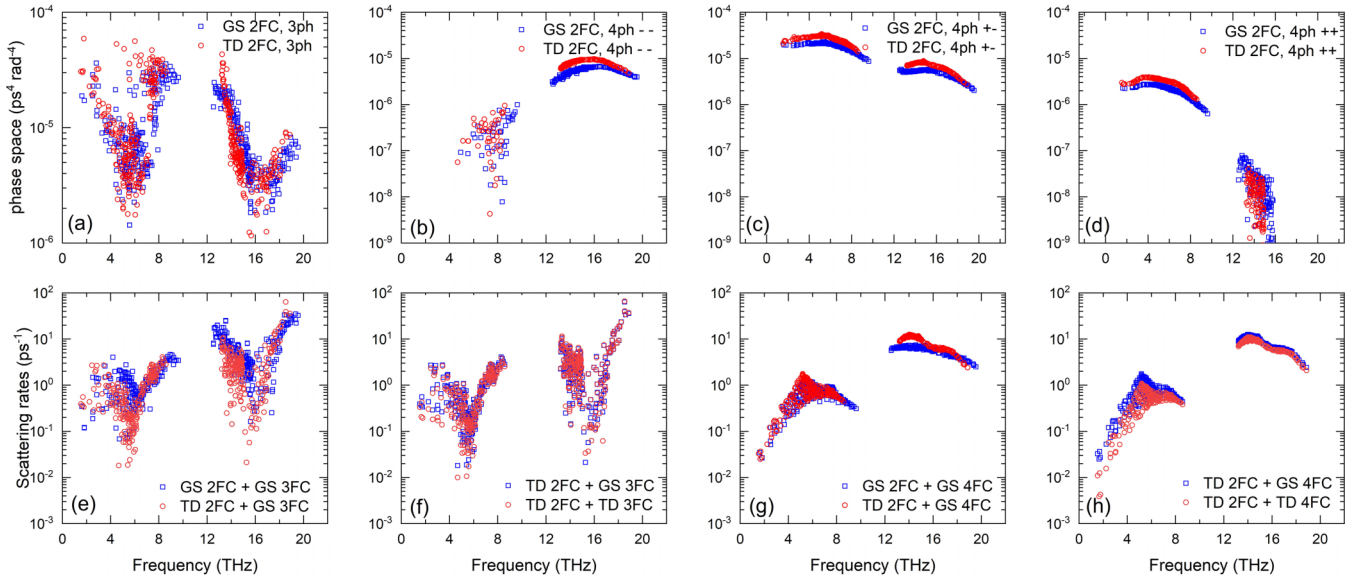
FIG. 5. Effects of GS and TD FC on 3ph and 4ph phase space and rates at 3000 K. (a) Effect of TD 2FC on 3ph phase space. (b)–(d) Effect of TD 2FC on 4ph phase space. (b) shows splitting 4ph processes ($\lambda_1 \rightarrow \lambda_2 + \lambda_3 + \lambda_4$). (c) shows redistribution 4ph processes ($\lambda_1 + \lambda_2 \rightarrow \lambda_3 + \lambda_4$). (d) shows recombination 4ph processes ($\lambda_1 + \lambda_2 + \lambda_3 \rightarrow \lambda_4$). (e) Effect of TD 2FC on 3ph rates. (f) Effect of TD 3FC on 3ph rates. (g) Effect of TD 2FC on 4ph rates. (h) Effect of TD 4FC on 4ph rates.

cally as a result of the increase of electron-phonon scattering [34,67]. The σ calculated in this study is consistent with the results of stoichiometric ZrC obtained in Ref. [26] using *ab initio* molecular dynamics simulations. However, it should be noted that our σ prediction is higher than most of the experimental data, particularly at low temperatures. This could be because the DFT calculations assume a perfect crystal and do not consider the effects of defects (especially the carbon vacancies) and porosity that are present in experimental samples. This idea is supported by the findings in Ref. [26], where an increase in electrical resistivity (equivalently decrease in σ) is observed with impurities and

defects in the sample. Furthermore, the Lorenz number (L) using the Wiedemann-Franz law: $L = \kappa_{el}/\sigma T$ is calculated, which is found to deviate significantly from the Sommerfeld value of $2.44 \times 10^{-8}\,\mathrm{W\,\Omega\,K^{-2}}$ and vary from 1.6 to $3.3 \times 10^{-8}\,\mathrm{W\,\Omega\,K^{-2}}$ at different temperatures. This deviation from the standard value highlights the limitations of using the Lorenz number to calculate κ_{el} from σ, as such an approach can lead to overprediction at lower temperatures and underprediction at higher temperatures.

The κ_{el} is compared to κ_{ph} as a function of temperature in Fig. 8. Phonons dominate thermal transport at lower
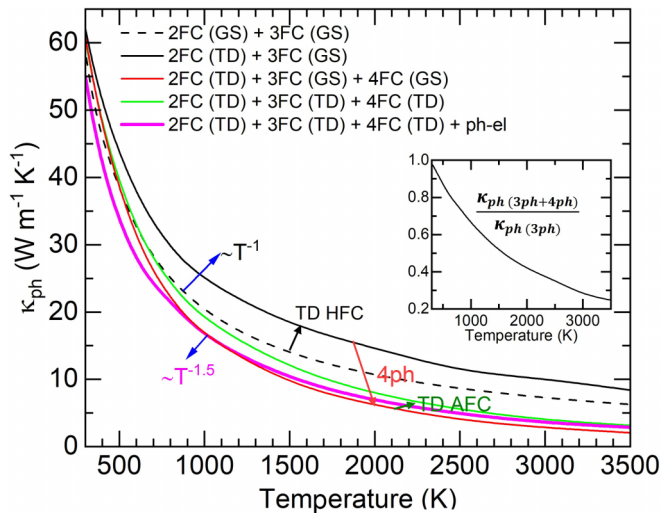

FIG. 6. Temperature-dependent phonon thermal conductivity of ZrC calculated using different scattering mechanisms. The inset shows the relative contribution of 4ph rates compared to 3ph rates.
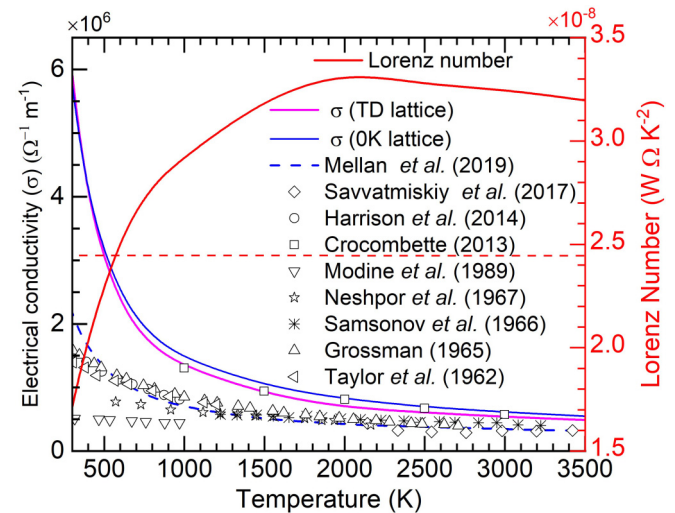

FIG. 7. Electrical conductivity and Lorenz number of ZrC as a function of temperature. Literature data of electrical conductivity (Mellan *et al.* [29], Savvatimskiy *et al.* [2], Harrison *et al.* [68], Crocombette [26], Modine *et al.* [69], Grossman [22], Taylor [18], Neshpor *et al.* and Samsonov *et al.* reproduced from Ref. [4]), are included for comparison.
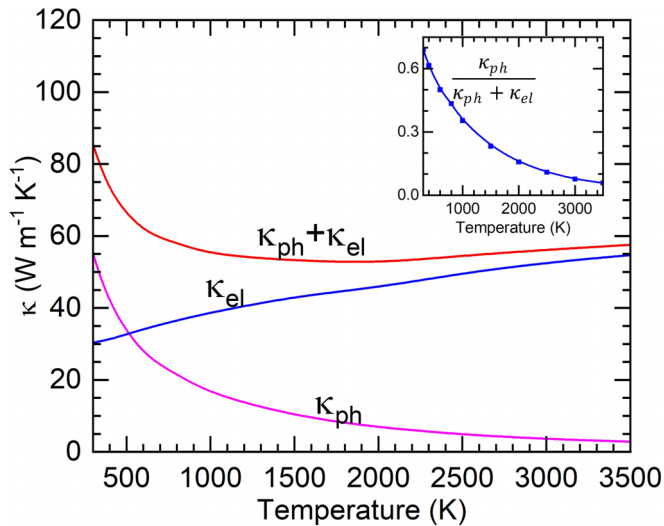
FIG. 8. Temperature-dependent κ_{ph}, κ_{el}, and κ of ZrC. The inset shows the relative contribution of κ_{ph}.

temperatures whereas electrons dominate at higher temperatures, similar to results found in Refs. [26,29,70]. As temperature increases, e.g., from 300 to 3500 K, κ_{el} increases from 30 to 54.7 W m^{-1} K^{-1}, whereas κ_{ph} decreases from 55.0 to 2.9 W m^{-1} K^{-1}. At room temperature, κ_{ph} accounts for roughly 70% of κ, which declines to just about 35% and 10% at 1000 and 3500 K, respectively.

In Fig. 9, the predicted κ ($= \kappa_{ph} + \kappa_{el}$) is compared to various experimental data. The blue-shaded and pink-shaded regions represent the contribution of κ_{el} and κ_{ph}, respectively. We can find that the experimental data are scattered and considerably lower than our prediction. This should be due to the presence of various defects, porosity, and vacancies in the experimental samples, which significantly decrease κ. Carbon vacancy is known to inevitably present in ZrC due to the intrinsic thermodynamic instability [71,72]. This decrease is much more significant at lower temperatures compared to
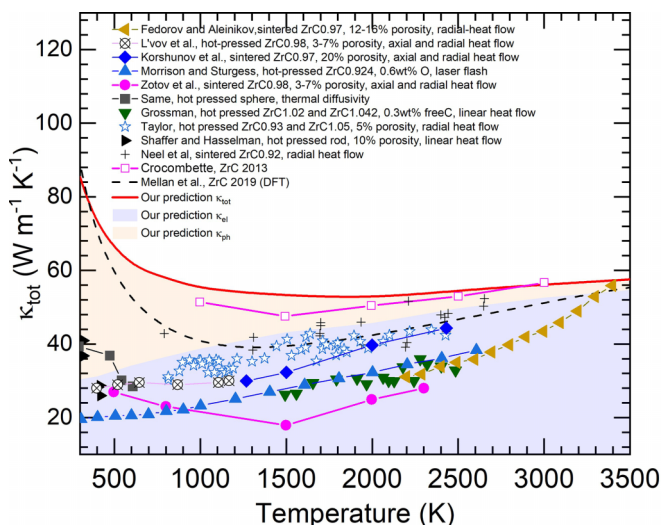

FIG. 9. Comparison of our predicted thermal conductivity with various literature data collected by Jackson and Lee [4], and theoretical prediction by *ab initio* molecular dynamics [26] and DFT [29].

higher temperatures due to the suppression of κ_{ph}. κ_{el} also gets suppressed due to impurities, defects, and vacancy scattering; however, the effect is smaller as found by Crocombette [26] through molecular dynamics. In that study, the predicted κ for stoichiometric ZrC was much higher than the reported experimental data. However, when some vacancy was introduced, both κ_{el}, and κ_{ph} decreased, and the predicted κ matched the experimental data. It is worth noting that our κ, as well as κ_{el}, matches Crocombette's [26] results with good accuracy.

We also compare our results to those predicted in Ref. [29] by first principles. We find that they underpredict κ_{el} and overpredict κ_{ph}. As a result, their total κ prediction agrees with ours at low and ultrahigh temperatures, but is lower than ours in the intermediate temperature range, from 500 to 3000 K. In Ref. [29], at the temperature of 1500 K, κ_{ph} is overestimated by $\sim 27.5\%$ (9.93 $\rightarrow$ ~ 12.67 W m^{-1} K^{-1}), and κ_{el} is underestimated by $\sim 38\%$ (43.21 $\rightarrow$ $\sim$ 26.78 W m^{-1} K^{-1}), leading to κ underestimation of $\sim 25.81\%$ (53.15 $\rightarrow$ ~ 39.43 W m^{-1} K^{-1}). At ultrahigh temperatures of 3500 K, κ_{ph} is overestimated by $\sim 75\%$ and κ_{el} is underestimated by $\sim 8\%$, leading to a slight κ underestimation of $\sim 4\%$. At lower temperatures of 300 K, κ_{ph} is overestimated by $\sim 26.5\%$ and κ_{el} is underestimated by $\sim 50.6\%$, leading to a slight κ underestimation of $\sim 1.0\%$. The matching of the predicted κ in Ref. [29] with experimental data is due to the error-cancellation effect where the prediction underpredicts the κ and the experimental samples' defects reduce κ.

F. Effect of extrinsic defects and grain boundary

To understand the effect of extrinsic factors such as grain size, we calculate the cumulative thermal conductivity with respect to the mean free path (MFP). As shown in Fig. 10(a), in bulk ZrC, 80% of κ_{ph} at 300, 1000, and 3000 K is contributed by the phonons with an MFP of less than 300, 60, and 20 nm, respectively. The effect of grain boundaries on thermal conductivity is more pronounced at lower temperatures. The MFP of electrons is much smaller than that of phonons. Eighty percent of heat transfer occurs with electrons having MFPs less than 15, 4, and 0.7 nm. This suggests that the contribution of grain boundary scattering is much less significant for electrons compared to phonons. Figure 10(b) shows the normalized κ_{ph} as a function of grain size from 10 to 10 000 nm. The solid line represents the current method (TDFC, 3ph + 4ph), while the dashed line represents the traditional approach (GSFC, 3ph). The graph explains how much κ_{ph} gets suppressed (in terms of percent) at various grain sizes and temperatures. For instance, if the grain boundary size is 100 nm, the κ_{ph} at 300, 1000, 2000, and 3000 K is roughly 55%, 76%, 87%, and 94% of the bulk values, respectively. The inset shows the grain size required to reduce κ_{ph} to 80% of the bulk values. At 300 and 3500 K, such grain sizes are 445 and 25 nm, respectively. The difference in grain boundary scattering between TDFC and GSFC is not substantial. Since the grain size in the experimental samples [2,4] is on the order of µm (~ 2 to 20 µm), the grain boundary scattering might not be the primary reason behind κ_{ph} suppression.

The impact of carbon and zirconium vacancies on κ_{ph} of ZrC is calculated and found to be strong, using perturbation theory, as shown in Fig. 11(a). For example, at 300 K, 1%
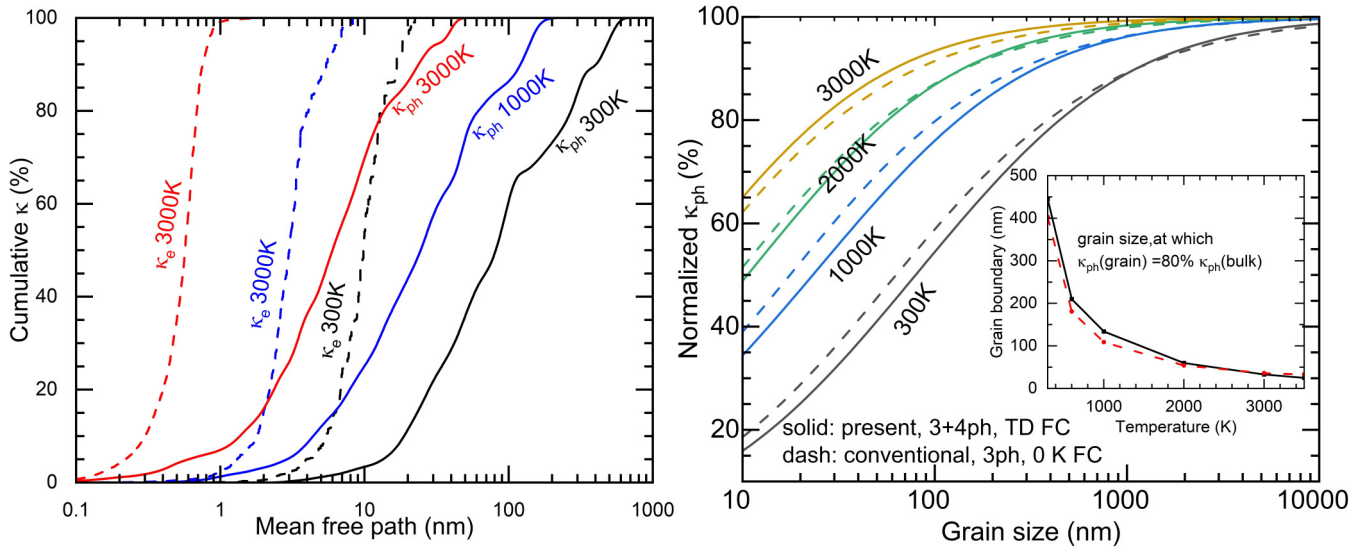
FIG. 10. (a) Cumulative κ_{ph} and κ_{el} with mean free path at various temperatures. (b) Percentage normalized κ_{ph} as a function of grain size. The inset shows the grain size at which κ_{ph} is 80% of the bulk value.

and 2% carbon vacancies can decrease κ_{ph} by 39% and 56%, respectively. The impact of Zr vacancy is even stronger; e.g., at 300 K, even 0.5% of Zr vacancy can lead to a decrease in κ_{ph} by 80%. This can be explained by the partial density of states presented in Fig. 3. Zr has a much larger mass than C and dominates the acoustic frequency bands, which dominate the heat transfer. A small concentration of Zr vacancy can lead to a significant decrease in κ_{ph}.

Figure 11(b) displays κ of ZrC for various C/Zr ratios, with experimental data collected by Jackson and Lee [4] and DFT prediction by Mellan *et al.* [29]. The figure reveals that the experimental κ increases exponentially as the crystal structure approaches the stoichiometric ratio, which is in line with the trend predicted by DFT. It is worth noting that our prediction

accounts only for the κ_{ph} suppression caused by C and Zr vacancies. If we include the κ_{ph} and κ_{el} suppression due to impurities, porosity, and grain boundaries as well, we can safely assume that our prediction will become lower and approaches the experimental value. This suggests that the experimental κ value does not reach the maximum theoretical limit of κ of ZrC, as κ_{ph} and κ_{el} are suppressed by the presence of vacancies, impurities, grain boundaries, and porosity in the sample.

IV. CONCLUSIONS

In this study, the thermal transport of ZrC is predicted using the first-principles calculations. Various factors affecting
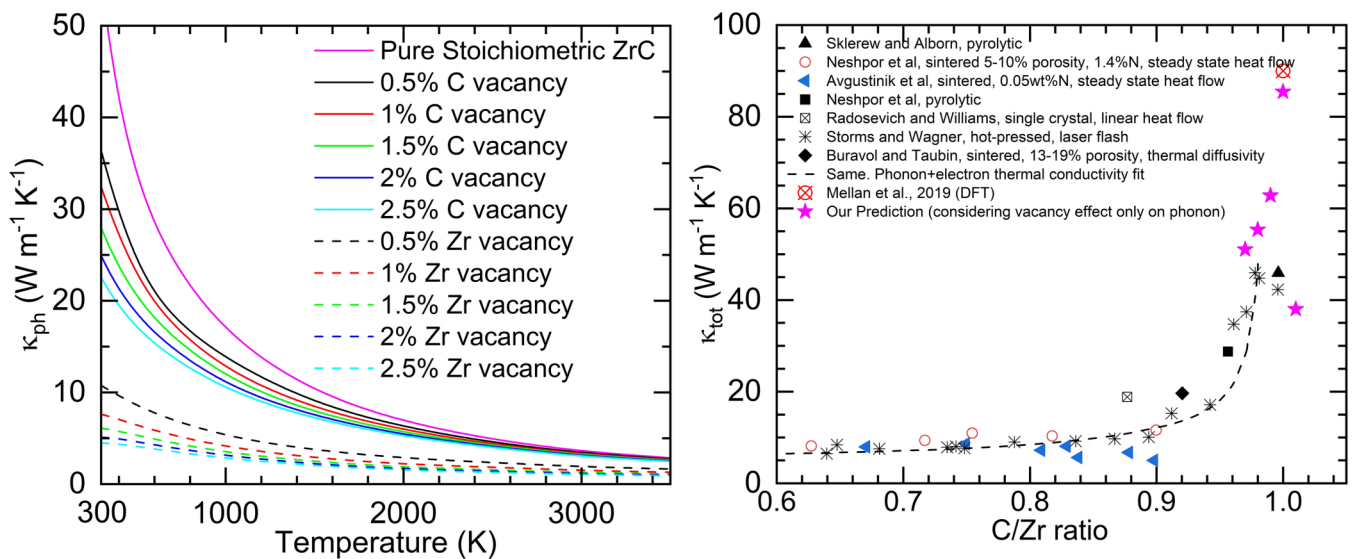

FIG. 11. (a) Effect of C and Zr vacancy on phonon thermal conductivity of ZrC. (b) Variation of total thermal conductivity of ZrC with different C/Zr ratios. DFT prediction by Mellan *et al.* [29] and various experimental data collected by Jackson and Lee [4] are presented for comparison.

thermal transport, especially at high temperatures, are considered, including high-order phonon scattering, lattice expansion, TDFC, and interband phonon conduction. The following conclusions can be drawn. (1) TD bulk modulus and TDFC are important for the accurate prediction of TEC at high temperatures. (2) Phonons and electrons dominate the heat transfer at lower and higher temperatures, respectively. κ_{ph} contributes roughly 70% at room temperature and declines to about 35% and 10% when the temperature increases to 1000 and 3500 K, respectively. (3) The 4ph is important at high temperatures and reduces κ_{ph} by 2%, 34%, 59%, and 76% at 300, 1000, 2000, and 3500 K, respectively. (4) Although the electron-phonon scattering increases with temperature, its impact is much smaller than 3ph and 4ph scattering. (5) Interestingly, TD 2FC decreases 3ph rates but increases 4ph rates by decreasing and increasing the scattering phase spaces, respectively. For 4ph phase space, the TD 2FC flattens phonon bands, and allows more redistribution 4ph processes ($\lambda_1 + \lambda_2 \rightarrow \lambda_3 + \lambda_4$) to happen. (6) We confirm that the TD 3FC and 4FC decrease the phonon scattering cross section at elevated temperatures and increase the κ_{ph} significantly in metals (by 52% at 3500 K), in addition to that found in insulators [32]. (7) The combination effect of TD 2FC and TD 4FC reduces 4ph rates of acoustic modes but increases those of optical modes. (8) The maximum Wigner off-diagonal (diffuson) contribution to κ_{ph} (0.2 W m^{-1} K^{-1}) is much lower compared to standard Peierls phonon contribution κ_{ph} (2.9 W m^{-1} K^{-1} at 3500 K). (9) The σ decreases monotonically while κ_{el} increases as temperature increases. The Lorenz number (L) deviates significantly from the Sommerfeld value of $L_0 = 2.44 \times 10^{-8}$ W Ω K^{-2}, highlighting the limitations of using the L_0 to calculate κ_{el}. (10) No experimental data have reached the predicted intrinsic thermal conductivity values due to the presence of inherent defects in the experimental samples. The matching of κ predicted in the literature with experimental data is due to the error-cancellation effect where the prediction underpredicts the κ and the experimental samples' defects reduce κ. Overall, our study makes a critical revisit to the thermal transport from room to ultrahigh temperatures.

Source data are provided along with this paper. All other data that support the plots within this paper are available from the corresponding author on reasonable request. The codes used in this study are available from the corresponding author upon request.

[1] A. F. Guillermet, Analysis of thermochemical properties and phase stability in the zirconium-carbon system, J. Alloys Compd. **217**, 69 (1995).

[2] A. I. Savvatimskiy, S. V. Onufriev, and S. A. Muboyadzhyan, Measurement of ZrC properties up to 5000 K by fast electrical pulse heating method, J. Mater. Res. **32**, 1287 (2017).

[3] C. C. Sorrell, V. S. Stubican, and R. C. Bradt, Mechanical properties of ZrC−ZrB$_2$ and ZrC−TiB$_2$ directionally solidified eutectics, J. Am. Ceram. Soc. **69**, 317 (1986).

[4] H. F. Jackson and W. E. Lee, Properties and characteristics of ZrC, in *Comprehensive Nuclear Materials, Five Volume Set*, edited by R. J. M. Konings (Elsevier Inc., Amsterdam, 2012), Vol. 2, pp. 339–372.

[5] R. W. Harrison and W. E. Lee, Processing and properties of ZrC, ZrN and ZrCN ceramics: A review, Adv. Appl. Ceram. **115**, 294 (2016).

[6] D. Cheng, S. Wang, and H. Ye, First-principles calculations of the elastic properties of ZrC and ZrN, J. Alloys Compd. **377**, 221 (2004).

[7] D. Sciti, S. Guicciardi, and M. Nygren, Spark plasma sintering and mechanical behaviour of ZrC-based composites, Scr. Mater. **59**, 638 (2008).

[8] S. L. Wang, K. Z. Li, H. J. Li, Y. L. Zhang, and Y. J. Wang, Effects of Microstructures on the Ablation Behaviors of ZrC Deposited by CVD, Surf. Coatings Technol. **240**, 450 (2014).

[9] G. M. Song, Y. J. Wang, and Y. Zhou, Elevated temperature ablation resistance and thermophysical properties of tungsten matrix composites reinforced with ZrC particles, J. Mater. Sci. **36**, 4625 (2001).

[10] Q. Tong, J. Shi, Y. Song, Q. Guo, and L. Liu, Resistance to ablation of pitch-derived ZrC/C composites, Carbon **42**, 2495 (2004).

[11] M. B. Dickerson, P. J. Wurm, J. R. Schorr, W. P. Huffman, P. G. Wapner, and K. H. Sandhage, Near net-shape, ultra-high melting, recession-resistant ZrC/W-based rocket nozzle liners via the displacive compensation of porosity (DCP) method, J. Mater. Sci. **39**, 6005 (2004).

[12] Y. Xu, W. Sun, X. Xiong, F. Liu, and X. Luan, Ablation characteristics of mosaic structure ZrC-SiC coatings on low-density, porous C/C composites, J. Mater. Sci. Technol. **35**, 2785 (2019).

[13] A. Paul, S. Venugopal, J. Binner, B. Vaidhyanathan, D. D. Jayaseelan, E. Zapata-Solvas, W. E. Lee, A. Heaton, and P. Brown, UHTC composites for hypersonic applications, Am. Ceram. Soc. Bull. **91**, 22 (2012).

[14] Y. Katoh, G. Vasudevamurthy, T. Nozawa, and L. L. Snead, Properties of zirconium carbide for nuclear fuel applications, J. Nucl. Mater. **441**, 718 (2013).

[15] L. L. Snead, Y. Katoh, and S. Kondo, Effects of fast neutron irradiation on zirconium carbide, J. Nucl. Mater. **399**, 200 (2010).

[16] K. Schönfeld, M. Trache, and H. P. Martin, Electrical performance of ZrC ceramics, Materialwiss. Werkstofftech. **52**, 1338 (2021).

[17] A. V. Kostanovskiy, M. E. Kostanovskaya, M. G. Zeodinov, and A. A. Pronkin, Electrical resistivity of zirconium carbide at 1200–2500 K, J. Phys.: Conf. Ser. **1787**, 012008 (2021).

[18] R. E. Taylor, Thermal conductivity of zirconium carbide at high temperatures, J. Am. Ceram. Soc. **45**, 353 (1962).

[19] B. Wei, L. Chen, Y. Wang, H. Zhang, S. Peng, J. Ouyang, D. Wang, and Y. Zhou, Densification, mechanical and thermal properties of ZrC_{1-x} ceramics fabricated by two-step reactive hot pressing of ZrC and ZrH_2 powders, J. Eur. Ceram. Soc. **38**, 411 (2018).

[20] X. Wei, C. Back, O. Izhvanov, C. D. Haines, and E. A. Olevsky, Zirconium carbide produced by spark plasma sintering and hot pressing: Densification kinetics, grain growth, and thermal properties, Materials **9**, 577 (2016).

[21] R. E. Taylor and J. Morreale, Thermal conductivity of titanium carbide, zirconium carbide, and titanium nitride at high temperatures, J. Am. Ceram. Soc. **47**, 69 (1964).

[22] L. N. Grossman, High-temperature thermophysical properties of zirconium carbide, J. Am. Ceram. Soc. **48**, 236 (1965).

[23] M. H. Leipold and T. H. Nielson, Mechanical properties of hot-pressed zirconium carbide tested to 2600°C, NASA Technical Report No. 19640040628 (1964).

[24] R. E. B. Makinson, The thermal conductivity of metals, Math. Proc. Cambridge Philos. Soc. **34**, 474 (1938).

[25] E. Grüneisen and H. Reddemann, Elektronen- und gitterleitung beim wärmefluß in metallen, Ann. Phys. **412**, 843 (1934).

[26] J. P. Crocombette, Origins of the high temperature increase of the thermal conductivity of transition metal carbides from atomistic simulations, J. Phys.: Condens. Matter **25**, 505501 (2013).

[27] Y. Zhou, W. G. Fahrenholtz, J. Graham, and G. E. Hilmas, From thermal conductive to thermal insulating: Effect of carbon vacancy content on lattice thermal conductivity of ZrC_x, J. Mater. Sci. Technol. **82**, 105 (2021).

[28] Y. Zhou, W. G. Fahrenholtz, J. Graham, and G. E. Hilmas, Electronic structure and thermal conductivity of zirconium carbide with hafnium additions, J. Am. Ceram. Soc. **104**, 4708 (2021).

[29] T. A. Mellan, A. Aziz, Y. Xia, R. Grau-Crespo, and A. I. Duff, Electron and phonon interactions and transport in the ultrahigh-temperature ceramic ZrC, Phys. Rev. B **99**, 094310 (2019).

[30] T. Feng, L. Lindsay, and X. Ruan, Four-phonon scattering significantly reduces intrinsic thermal conductivity of solids, Phys. Rev. B **96**, 161201(R) (2017).

[31] X. Yang, T. Feng, J. Li, and X. Ruan, Stronger role of four-phonon scattering than three-phonon scattering in thermal conductivity of III-V semiconductors at room temperature, Phys. Rev. B **100**, 245203 (2019).

[32] X. Yang, J. Tiwari, and T. Feng, Reduced anharmonic phonon scattering cross-section slows the decrease of thermal conductivity with temperature, Mater. Today Phys. **24**, 100689 (2022).

[33] G. D. Mahan, *Many-Particle Physics* (Springer Science & Business Media, Berlin, 2000).

[34] Z. Tong, S. Li, X. Ruan, and H. Bao, Comprehensive first-principles analysis of phonon thermal conductivity and electron-phonon coupling in different metals, Phys. Rev. B **100**, 144306 (2019).

[35] C. A. Ratsifaritana and P. G. Klemens, Scattering of phonons by vacancies, Int. J. Thermophys. **8**, 737 (1987).

[36] G. Xie, Y. Shen, X. Wei, L. Yang, H. Xiao, J. Zhong, and G. Zhang, A bond-order theory on the phonon scattering by vacancies in two-dimensional materials, Sci. Rep. **4**, 5085 (2014).

[37] B. Xu, T. Feng, Z. Li, S. T. Pantelides, and Y. Wu, Constructing highly porous thermoelectric monoliths with high-performance and improved portability from solution-synthesized shape-controlled nanocrystals, Nano Lett. **18**, 4034 (2018).

[38] See Supplemental Material at http://link.aps.org/supplemental/10.1103/PhysRevMaterials.7.065001 for thermal conductivity convergence with respect to q-mesh, three and four-phonon scattering rates as a function of temperature, effects of temperature-dependent force constants, 4ph, isotope, and phonon-electron scattering rate on phonon thermal conductivity, vacancy and grain boundary scattering, electron band structure, electron scattering rates, and 3ph scattering rates.

[39] G. Kresse and J. Hafner, *Ab initio* molecular dynamics for liquid metals, Phys. Rev. B **47**, 558 (1993).

[40] G. Kresse and J. Furthmüller, Efficiency of *ab-initio* total energy calculations for metals and semiconductors using a plane-wave basis set, Comput. Mater. Sci. **6**, 15 (1996).

[41] G. Kresse and D. Joubert From ultrasoft pseudopotentials to the projector augmented-wave method, Phys. Rev. B **59**, 1758 (1999).

[42] J. P. Perdew, K. Burke, and M. Ernzerhof, Generalized Gradient Approximation Made Simple, Phys. Rev. Lett. **77**, 3865 (1996).

[43] A. Togo and I. Tanaka, First principles phonon calculations in materials science, Scr. Mater. **108**, 1 (2015).

[44] W. W. Li, J. Carrete, N. A. Katcho, and N. Mingo, SHENGBTE: A solver of the Boltzmann transport equation for phonons, Comput. Phys. Commun. **185**, 1747 (2014).

[45] O. Hellman, I. A. Abrikosov, and S. I. Simak, Lattice dynamics of anharmonic solids from first principles, Phys. Rev. B **84**, 180301(R) (2011).

[46] O. Hellman, P. Steneteg, I. A. Abrikosov, and S. I. Simak, Temperature dependent effective potential method for accurate free energy calculations of solids, Phys. Rev. B **87**, 104111 (2013).

[47] S. Baroni, P. Giannozzi, and A. Testa, Greens-Function Approach to Linear Response in Solids, Phys. Rev. Lett. **58**, 1861 (1987).

[48] S. Baroni, S. De Gironcoli, A. Dal Corso, and P. Giannozzi, Phonons and related crystal properties from density-functional perturbation theory, Rev. Mod. Phys. **73**, 515 (2001).

[49] X. Gonze and C. Lee, Dynamical matrices, Born effective charges, dielectric permittivity tensors, and interatomic force constants from density-functional perturbation theory, Phys. Rev. B **55**, 10355 (1997).

[50] S. Poncé, E. R. Margine, C. Verdi, and F. Giustino, EPW: Electron–phonon coupling, transport and

superconducting properties using maximally localized Wannier functions, Comput. Phys. Commun. **209**, 116 (2016).

[51] F. Giustino, M. L. Cohen, and S. G. Louie, Electron-phonon interaction using Wannier functions, Phys. Rev. B **76**, 165108 (2007).

[52] E. R. Margine and F. Giustino, Anisotropic Migdal-Eliashberg theory using Wannier functions, Phys. Rev. B **87**, 024505 (2013).

[53] J. Noffsinger, F. Giustino, B. D. Malone, C.-H. Park, S. G. Louie, and M. L. Cohen, EPW: A program for calculating the electron-phonon coupling using maximally localized Wannier functions, Comput. Phys. Commun. **181**, 2140 (2010).

[54] P. Giannozzi *et al.*, QUANTUM ESPRESSO: A modular and open-source software project for quantum simulations of materials, J. Phys.: Condens. Matter **21**, 395502 (2009).

[55] P. Giannozzi *et al.*, Advanced capabilities for materials modelling with QUANTUM ESPRESSO, J. Phys.: Condens. Matter **29**, 465901 (2017).

[56] A. A. Mostofi, J. R. Yates, G. Pizzi, Y.-S. Lee, I. Souza, D. Vanderbilt, and N. Marzari, An updated version of WANNIER90: A tool for obtaining maximally-localised Wannier functions, Comput. Phys. Commun. **185**, 2309 (2014).

[57] J. Zhang and J. M. McMahon, Temperature-dependent mechanical properties of ZrC and HfC from first principles, J. Mater. Sci. **56**, 4266 (2021).

[58] A. Abdollahi, First-principle calculations of thermodynamic properties of ZrC and ZrN at high pressures and high temperatures, Phys. B: Condens. Matter **410**, 57 (2013).

[59] A. C. Lawson, D. P. Butt, J. W. Richardson, and J. Li, Thermal Expansion and Atomic Vibrations of Zirconium Carbide to 1600 K, Philos. Mag. **87**, 2507 (2007).

[60] T. Feng, X. Yang, and X. Ruan, Phonon anharmonic frequency shift induced by four-phonon scattering calculated from first principles, J. Appl. Phys. **124**, 145101 (2018).

[61] P. T. Jochym and K. Parlinski, *Ab initio* lattice dynamics and elastic constants of ZrC, Eur. Phys. J. B **15**, 265 (2000).

[62] H. G. Smith, N. Wakabayashi, and M. Mostoller, Phonon anomalies in transition metals, alloys and compounds, in

Superconductivity in d- and f-Band Metals, edited by D. H. Douglass (Springer, Boston, MA, 1976), pp. 223–249.

[63] Y. Xia, Revisiting lattice thermal transport in PbTe: The crucial role of quartic anharmonicity, Appl. Phys. Lett. **113**, 073901 (2018).

[64] Y. Xia, V. I. Hegde, K. Pal, X. Hua, D. Gaines, S. Patel, J. He, M. Aykol, and C. Wolverton, High-Throughput Study of Lattice Thermal Conductivity in Binary Rocksalt and Zinc Blende Compounds Including Higher-Order Anharmonicity, Phys. Rev. X **10**, 041029 (2020).

[65] M. Simoncelli, N. Marzari, and F. Mauri, Wigner Formulation of Thermal Transport in Solids, Phys. Rev. X **12**, 041011 (2022).

[66] M. Simoncelli, N. Marzari, and F. Mauri, Unified theory of thermal transport in crystals and glasses, Nat. Phys. **15**, 809 (2019).

[67] S. Li, Z. Tong, X. Zhang, and H. Bao, Thermal conductivity and Lorenz ratio of metals at intermediate temperatures with mode-level first-principles analysis, Phys. Rev. B **102**, 174306 (2020).

[68] R. Harrison, O. Ridd, D. D. Jayaseelan, and W. E. Lee, Thermophysical characterisation of ZrC_xN_y ceramics fabricated via carbothermic reduction-nitridation, J. Nucl. Mater. **454**, 46 (2014).

[69] F. A. Modine, M. D. Foegelle, C. B. Finch, and C. Y. Allison, electrical properties of transition-metal carbides of group IV, Phys. Rev. B **40**, 9558 (1989).

[70] X. Gu, S. Li, and H. Bao, Thermal conductivity of silicon at elevated temperature: Role of four-phonon scattering and electronic heat conduction, Int. J. Heat Mass Transfer **160**, 120165 (2020).

[71] Y. Zhou, T. W. Heitmann, W. G. Fahrenholtz, and G. E. Hilmas, Synthesis of ZrC_x with controlled carbon stoichiometry by low temperature solid state reaction, J. Eur. Ceram. Soc. **39**, 2594 (2019).

[72] Y. Zhou, T. W. Heitmann, E. Bohannan, J. C. Schaeperkoetter, W. G. Fahrenholtz, and G. E. Hilmas, Carbon vacancy ordering in zirconium carbide powder, J. Am. Ceram. Soc. **103**, 2891 (2020).

Janak Tiwari, Tianli Feng*

Department of Mechanical Engineering, University of Utah, Salt Lake City, UT 84112, USA

Corresponding Author:

*tianli.feng@utah.edu

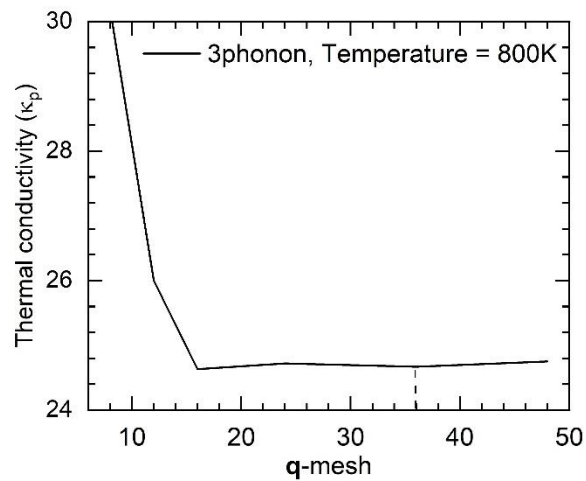### A. Thermal conductivity convergence with respect to q-mesh

Figure S1: **q**-mesh convergence analysis of ShengBTE calculation. 3ph was taken to be converged at **q**-mesh of 36×36×36.

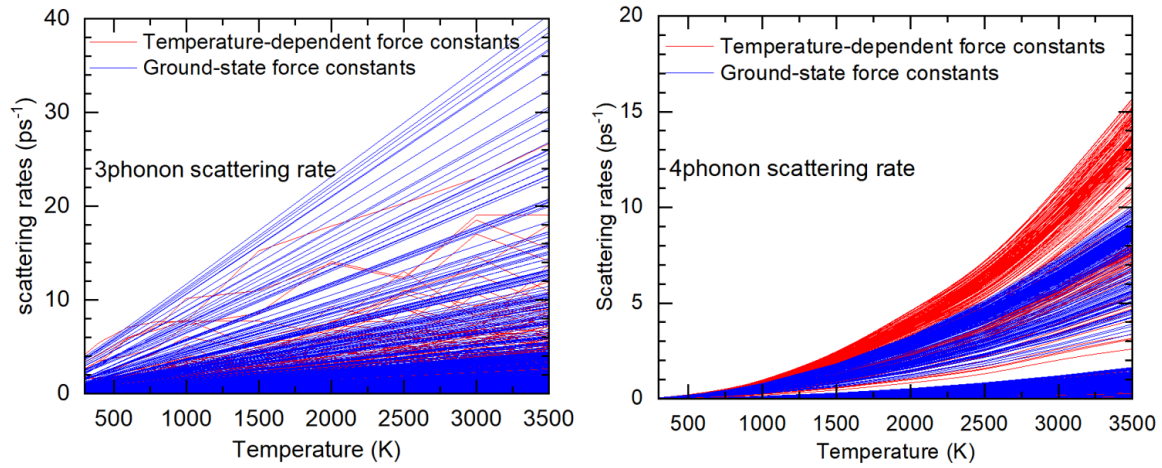## B. Three and four-phonon scattering rates as a function of temperature

Figure S2: (a) 3ph and (b) 4ph scattering rates of ZrC at various temperatures. The blue line and red line represent the scattering rates calculated using ground-state force constants and temperature-dependent force constants respectively.

C. Effects of Temperature-dependent force constants, 4ph, isotope, and phonon-electron scattering rate on phonon thermal conductivity

Legend:

G+G = 2nd FC (GS) + 3rd FC (GS)
T+G = 2nd FC (GS) + 3rd FC (TD)
T+T = 2nd FC (TD) + 3rd FC (TD)
G+G+G = 2nd FC (GS) + 3rd FC (GS) + 4th FC (GS)
T+G+G = 2nd FC (TD) + 3rd FC (GS) + 4th FC (GS)
T+T+T = 2nd FC (TD) + 3rd FC (TD) + 4th FC (TD)
T+T+T (no isotope) = isotope free 2nd FC (TD) + 3rd FC (TD) + 4th FC (TD)
T+T+T + ph-el = 2nd FC (GS) + 3rd FC (GS) + 4th FC (GS) + phonon-electron scattering
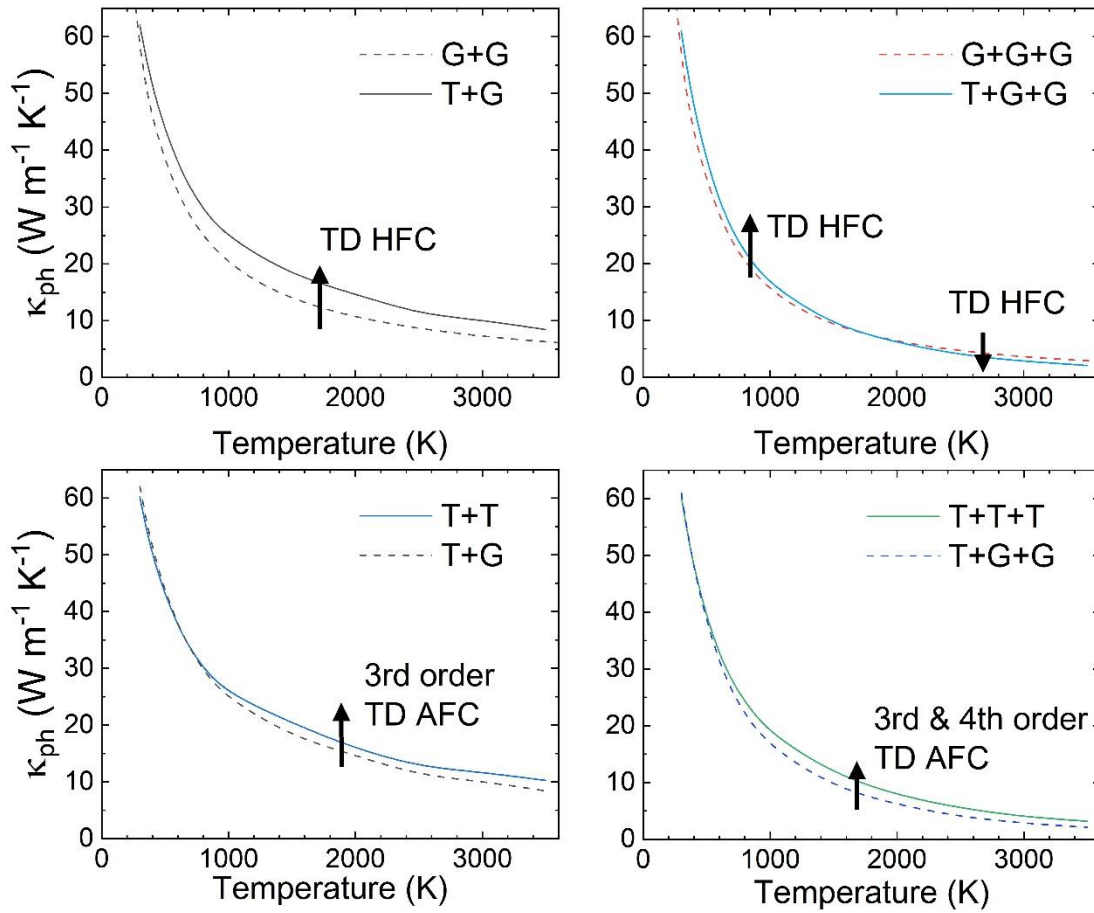
a. Temperature-dependent force constants

Figure S3: Effect of temperature-dependent harmonic and anharmonic force constants on phonon thermal conductivity of ZrC at various temperatures.

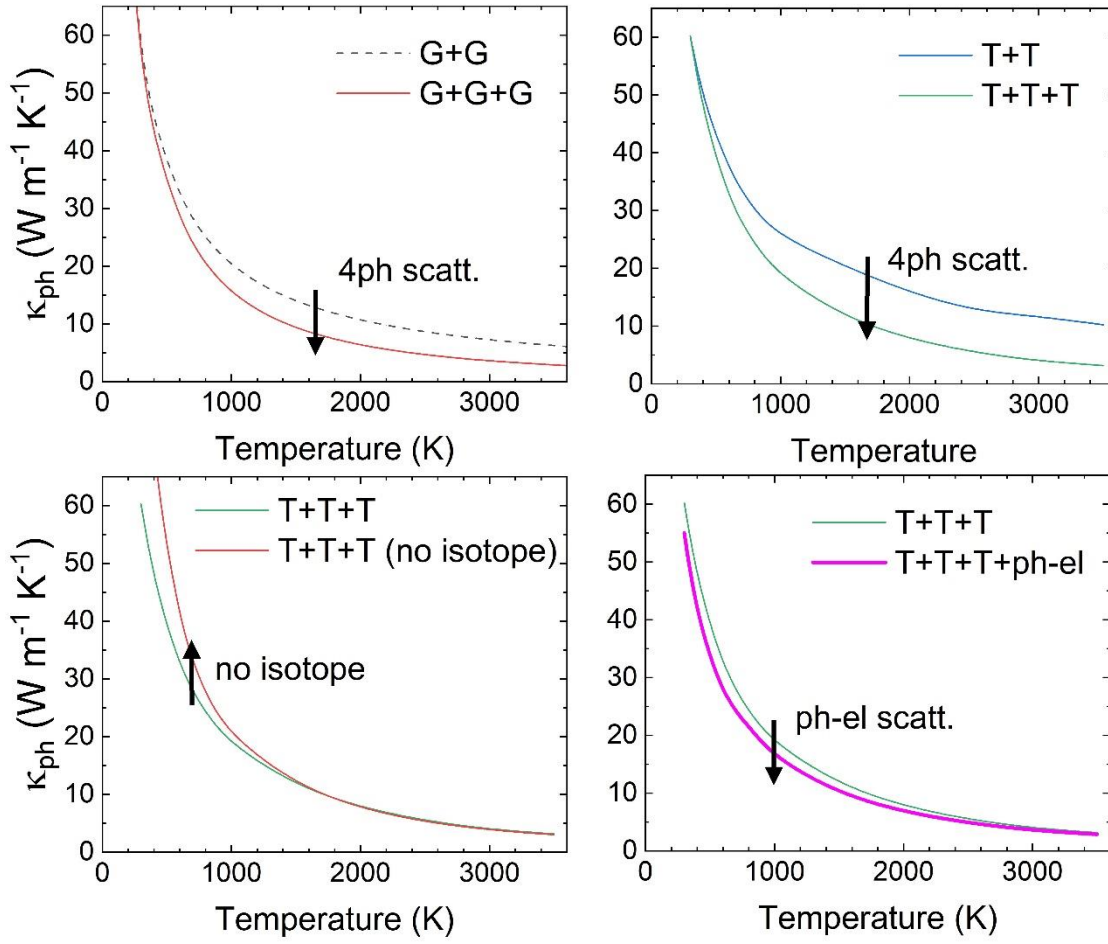## b. 4 phonon, isotope, and phonon-electron scattering rate

Figure S4: Effects of 4phonon scatterings, isotope scatterings, and phonon-electron scattering on phonon thermal conductivity of ZrC at various temperatures.

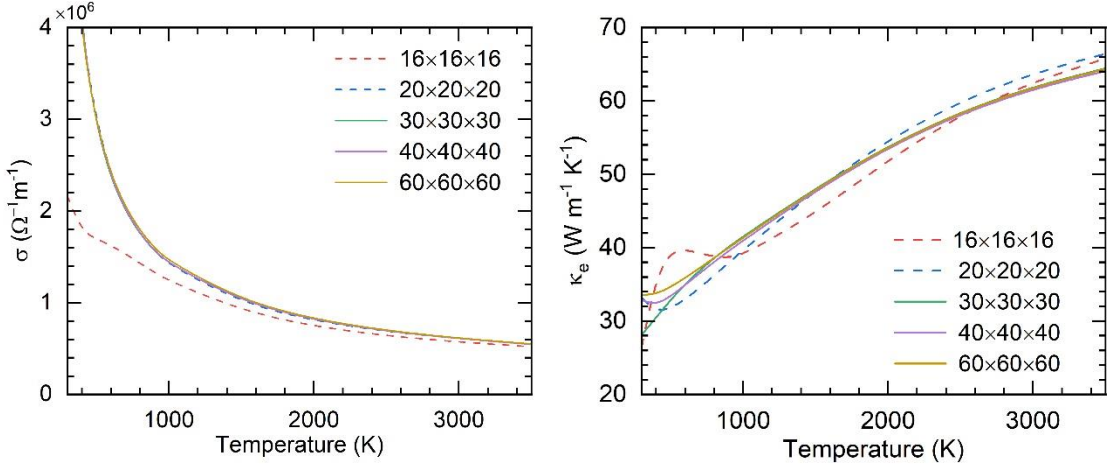## D. Convergence of q-mesh and k-mesh for electrical thermal conductivity calculation

Figure S5: Convergence analysis of k-mesh and q-mesh for electrical conductivity (left) and electron thermal conductivity (right).

E. Vacancy and grain boundary scattering

The scattering rates due to the grain boundary defects were calculated using equation S.1. Here, λ represents phonon mode $(\mathbf{q}, j)$ with $\mathbf{q}$ and j labeling the phonon wave vector and dispersion branch, respectively. $\tau_{gb,\lambda}$ represents the relaxation time of phonon at λ , v_{ph} represents the phonon group velocity, and D_{grain} is the grain size. The method used in the calculation was similar to as described in Ref.[1]

$$\tau_{gb,\lambda}^{-1} = \frac{v_{ph,\lambda}}{D_{grain}} \tag{S.1}$$

$$\tau_{d,\lambda}^{-1} = 9\frac{\pi}{2}f_v \cdot \left(1 - \frac{m_V}{m_b}\right)^2 \omega_\lambda^2 \cdot pDOS(\omega) \tag{S.2}$$

The scattering rate of the crystal with vacancy defects was estimated using equation S.2. In the equation, f_v represents the concentration of the vacancy (either Carbon vacancy or Zirconium vacancy); m_V represents the mass of the vacancy (which is equal to zero); and $\overline{m_b}$ represents the

mass of the basis atom (e.g., mass of Carbon for Carbon vacancy). Similarly, ω represents the angular velocities and $pDOS(\omega)$ represents the partial density of states of a basis atom. For example, to calculate the scattering rate of carbon vacancy, f_v is carbon vacancy, $\overline{m_b}$ is the atomic mass of carbon, and $pDOS(\omega)$ is the partial density of states of carbon atoms. The coefficient 9 in equation S.2 accounts for the mass and bond loss associated with the defect vacancy[2,3]. The $pDOS(\omega)$ of the atoms was calculated so that the weighted sum of $pDOS$ of all the atoms equals unity. The lattice thermal conductivity of the crystal with vacancy defect was then estimated based on the total scattering rate, which was obtained by summing defect scattering rates with intrinsic phonon scattering rates.
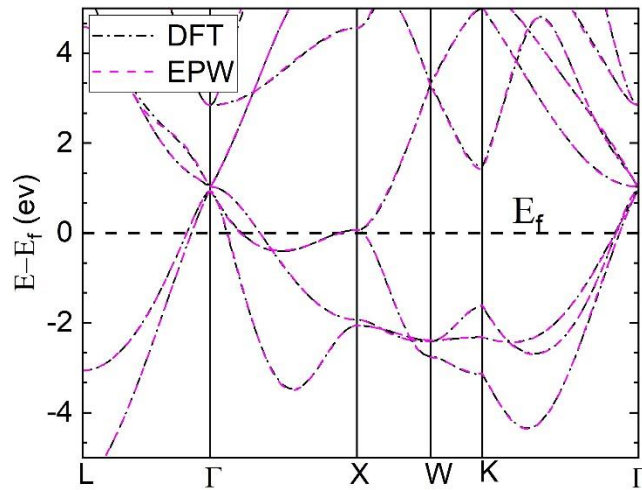
F. Electron band structure

Figure S6: The electron band structure of ZrC calculated by using EPW and Quantum Espresso separately. The dispersion obtained from both methods match well with each other.
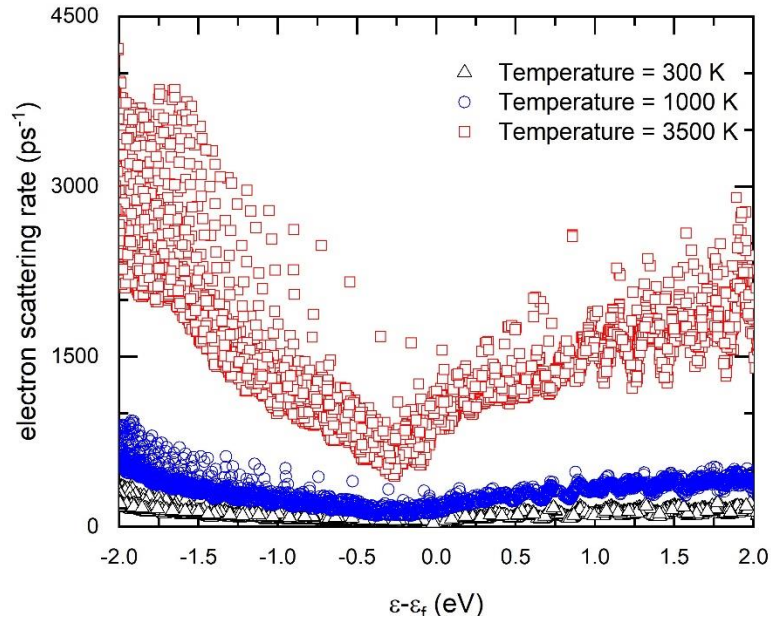
G. Electron scattering rates

Figure S7: Variation of electron-electron scattering rates of ZrC with temperature.

References:

(1)   Xu, B.; Feng, T.; Li, Z.; Pantelides, S. T.; Wu, Y. Constructing Highly Porous Thermoelectric Monoliths with High-Performance and Improved Portability from Solution-Synthesized Shape-Controlled Nanocrystals. *Nano Lett.* **2018**, *18* (6), 4034–4039. https://doi.org/10.1021/acs.nanolett.8b01691.

(2)   Ratsifaritana, C. A.; Klemens, P. G. Scattering of Phonons by Vacancies. *Int. J. Thermophys.* **1987**, *8*, 737–750.

(3)   Xie, G.; Shen, Y.; Wei, X.; Yang, L.; Xiao, H.; Zhong, J.; Zhang, G. A Bond-Order Theory on the Phonon Scattering by Vacancies in Two-Dimensional Materials. *Sci. Rep.* **2014**, *4* (1), 5085.